IET Microwaves, Antennas & Propagation

Research Article

Lens-coupled folded-dipole antennas for terahertz detection and imaging

ISSN 1751-8725
Received on 25th June 2014
Revised on 20th February 2015
Accepted on 24th March 2015
doi: 10.1049/iet-map.2014.0415
www.ietdl.org

Syed M. Rahman ✉, *Zhenguo Jiang*, *Huili (Grace) Xing*, *Patrick Fay*, *Lei Liu*

Department of Electrical Engineering, University of Notre Dame, 275 Fitzpatrick, IN, 46556, USA
✉ *E-mail: srahman@nd.edu*

Abstract: The authors report the design, simulation and characterisation of lens-coupled folded-dipole antennas (LC-FDAs) for terahertz (THz) detection and focal-plane imaging arrays. LC-FDAs operating at 200 GHz have been designed on semi-insulating silicon wafers with a resistivity larger than 20 000 Ω·cm. Even–odd mode analysis (EOA) has been performed to extract the currents of the two modes. The embedding impedance of the designed LC-FDAs has been simulated using conventional numerical electromagnetics, and the results show that a wide range of impedance values (both real and imaginary parts) can be achieved by changing the antenna geometry. This property makes LC-FDAs suitable for high-performance THz detectors in which impedance matching between antennas and devices is desired. From the currents calculated using EOA, the LC-FDA far-field radiation patterns, antenna directivity and Gaussian coupling efficiency for different lens structures have been examined using ray-tracing techniques. Good agreement between calculation results and measurement has been observed demonstrating the effectiveness of the above analysis approach. The single element FDA design has also been explored for use in high-resolution two-dimensional THz focal plane arrays by optimising the lens structure and evaluating the off-axis radiation patterns.

1 Introduction

Terahertz (THz, 0.1–10 THz) detection and imaging has become very attractive for a wide range of emerging applications including radio astronomy, atmospheric research, chemical spectroscopy, biological sensing, medical imaging, security screening and defence [1–9]. These applications are driving the demand for advanced detectors and imaging systems with technical features, such as high responsivity, low noise, high resolution and high speed while at the same time being physically compact and low cost. However, as the frequency increases into the THz region, the detection of RF signals becomes quite challenging largely because of difficulties associated with extending classical microwave technologies and techniques to this frequency regime. For example, the loss introduced by metallic waveguide increases with the frequency. In addition, tolerances associated with machining small waveguide structures become increasingly difficult to fulfil in fabricating waveguide circuits for use at THz frequencies, which also increases the cost significantly. An alternative approach based on quasi-optical technology has proven to be suitable for THz detection and imaging applications. As shown in Fig. 1, the 'reverse microscope' quasi-optical configuration is often used for THz detector or imaging array design in which a planar antenna or antenna array is fabricated on a dielectric substrate [10–16]. In order to reduce the coupling loss because of surface waves, an extended hemispherical dielectric lens (same dielectric constant as the antenna substrate) is often mounted to the antenna substrate (a lens-coupled antenna). The geometry of the dielectric lens (including the lens radius/diameter and extension length) needs to be optimised to provide good coupling efficiency and antenna directivity.

A variety of lens-coupled planar antennas including bow-tie antennas [17], double-slots [18], annular-slots [19, 20], sinuous and log-periodic antennas [21] have been employed on the basis of the 'reverse microscope' configuration to realise THz direct and heterodyne detectors [22]. However, these planar antenna structures tend to have relatively low embedding impedances (i.e. <100 Ω). On the other hand, room-temperature detectors and imaging focal-plane arrays (FPAs) have been demonstrated at THz frequencies using semiconductor devices, such as Schottky diodes and heterostructure backward diodes (HBDs) [23–25]. These devices typically present high impedances (both real and imaginary parts) at frequencies (~1 THz) below their cutoff frequencies. Since the state-of-the art Schottky diodes and HBDs can have cutoff frequencies well above 8 THz [23], these technologies are well-suited for THz detection and imaging applications. However, because of the substantial impedance mismatch between devices and low-impedance planar antennas, the power coupling efficiency is limited, resulting in relatively low detector performance. Although impedance matching networks can be utilised, this unavoidably leads to large circuit footprints, complex systems and reduced detection bandwidth. To overcome these issues, lens-coupled planar antennas that can potentially achieve high embedding impedances are needed for realising high-performance, room-temperature THz detectors and imaging FPA elements.

Planar folded-dipole antennas (FDAs) are known to have a high embedding impedance, and this impedance depends on the number of arms N [26]. Conventional FDAs consist of a closed loop, which also results in a DC short circuit at the output, making them not well suited for detection applications. An alternative planar FDA design with an open geometry, as shown in Fig. 1, has been proposed and demonstrated for enhancing output power from THz photomixers because of the improved impedance matching [27–29]. In addition, some preliminary Schottky-diode-based detector designs using lens-coupled planar FDAs (LC-FDAs) have been demonstrated experimentally at 75 and 200 GHz, showing promising performance [25, 30]. Unfortunately, to date, the RF parameters of LC-FDAs at THz frequencies, such as embedding impedance, far-field radiation pattern, directivity and Gaussian coupling efficiency have not yet been fully studied and documented. This is partially because of the difficulties associated with analysing, testing and characterising this kind of antennas, especially in the THz region.

In this paper, we present the design, simulation, analysis and testing of LC-FDAs at 200 GHz for THz detection and imaging applications. Even–odd mode analysis (EOA) was first performed to extract the related mode currents [26]. On the basis of the EOA,

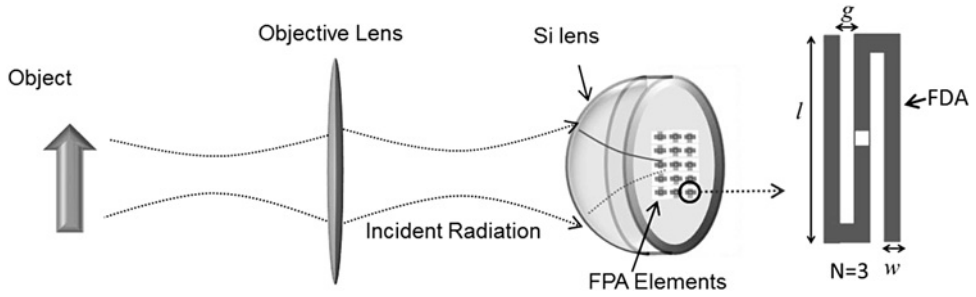

Fig. 1 *Reverse microscope configuration of folded-dipole antenna mounted on extended hemispherical silicon lens*

the antenna embedding impedance was evaluated and compared with ANSYS high frequency structure simulator (HFSS) simulation results. The results show the effectiveness of the EOA analysis approach. HFSS simulation also demonstrated that a wide range of impedance values (both real and imaginary parts) can be achieved by changing the antenna geometry. This unique property makes LC-FDAs suitable for impedance matching to a variety of devices (e.g. Schottky diodes and HBDs), without additional matching networks, to realise high performance, compact THz detectors and FPAs. In addition, the antenna far-field radiation patterns, antenna directivity and Gaussian coupling efficiency have been studied on the basis of the extracted mode currents (from the EOA analysis) using ray-tracing techniques. Good agreement between calculated results and measurements has been obtained, demonstrating the effectiveness of this analysis approach. Finally, the use of FDAs in full two-dimensional (2D) THz FPAs with high imaging resolution was explored by optimising the lens geometry and evaluating the off-axis radiation patterns of the FPAs.

2 Even-Odd-Mode Analysis of FDA

To analyse the LC-FDA (see Fig. 1), EOA has been performed [31]. This technique makes use of the physical symmetry of the FDA. As shown in Fig. 2, the analysis begins by decomposing the current components of the FDA into two distinct modes, namely, even-mode and odd-mode. By applying EOA, the single-port FDA with N arms can be decomposed into even-mode and odd-mode N-port networks. The solution of the original single-port problem can be treated as a superposition of the solutions of the two N-port sub-problems. This approach permits the direct calculation of the embedding impedance and radiation patterns of the LC-FDAs from the extracted mode currents.

As an example, an LC-FDA with a number of arms $N = 3$, antenna length of $l = 285$ μm, arm width $w = 12$ μm, arm gap $g = 12$ μm has been analysed from 150 to 250 GHz. Assuming the FDA is excited by a voltage V (1.0 V used in the analysis) at the feed point (middle of the centre antenna arm), the total current flowing through the antenna is I. Fig. 2 illustrates the decomposition of the FDA's feed point voltage V and total current I into even-mode and odd-mode using superposition theorem. The even-mode has

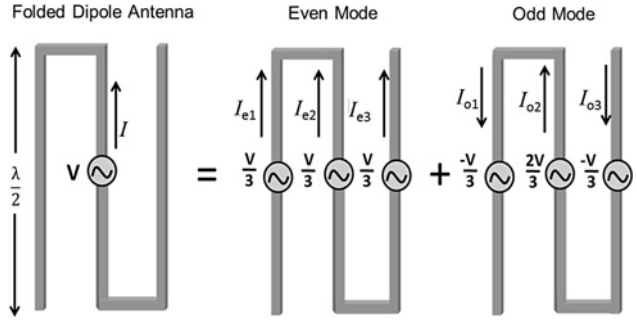

Fig. 2 *EOA: decomposition of folded-dipole antenna into even-mode and odd-mode circuits for extraction of the radiating antenna currents*

voltages $V/3$, $V/3$ and $V/3$ (from left to right) for the three ports, and the associated currents in three antenna arms are I_{e1}, I_{e2}, and I_{e3} respectively. Similarly, the odd-mode has voltages of $-V/3$, $2V/3$ and $-V/3$, and currents of I_{o1}, I_{o2} and I_{o3} in each arm. Since the FDA radiates largely from the even-mode currents and the parallel arms of the FDA cause the odd-mode currents to cancel out in the far field, the two mode currents are also called the radiation mode current and transmission line mode current, respectively [26]. The current and voltage for each mode can be related using a linear combination of the self and mutual impedances of the N-port network, where the ports are located at the centre of each arm. For the even-mode circuit, the resulting current and voltage equations are given by (for the case of $N = 3$)

$$\begin{bmatrix} \frac{V}{3} \\ \frac{V}{3} \\ \frac{V}{3} \end{bmatrix} = \begin{bmatrix} Z_{11} & Z_{12} & Z_{13} \\ Z_{21} & Z_{22} & Z_{23} \\ Z_{31} & Z_{32} & Z_{33} \end{bmatrix} \begin{bmatrix} I_{e1} \\ I_{e2} \\ I_{e3} \end{bmatrix} \tag{1}$$

where I_{e1}, I_{e2}, and I_{e3} are the even-mode terminal currents and $\boldsymbol{Z}$ represents the impedance matrix of the three-port network which has been computed using conventional full-wave simulations. For the odd-mode circuit, the relations are given by

$$\begin{bmatrix} \frac{-V}{3} \\ \frac{2V}{3} \\ \frac{-V}{3} \end{bmatrix} = \begin{bmatrix} Z_{11} & Z_{12} & Z_{13} \\ Z_{21} & Z_{22} & Z_{23} \\ Z_{31} & Z_{32} & Z_{33} \end{bmatrix} \begin{bmatrix} I_{o1} \\ I_{o2} \\ I_{o3} \end{bmatrix} \tag{2}$$

where I_{o1}, I_{o2} and I_{o3} represent the odd-mode terminal currents, and the $\boldsymbol{Z}$ matrix remains unchanged. Fig. 3*a* shows the resulting even-mode currents for this example FDA for a frequency range from 150 to 250 GHz. At the resonant frequency, the antenna radiates from the real part of the even-mode currents and provides distortionless radiation patterns [26]. The detailed computation of the far-field radiation patterns using the even-mode currents will be described in Section 4.

Once the mode currents (both even-mode and odd-mode) are determined, the embedding impedance (Z_{in}) of the FDAs (at the feed point of the original antenna problem shown in Fig. 2*a*) can be calculated from the current ratios and impedance matrix. The resulting equation for Z_{in} is given by

$$Z_{in} = \frac{V}{I_2} = \frac{I_1}{I_2} Z_{21} + Z_{22} + \frac{I_3}{I_2} Z_{23} \tag{3}$$

where $I_1 = I_{e1} + I_{o1}$, $I_2 = I_{e2} + I_{o2}$ and $I_3 = I_{e3} + I_{o3}$. Using the above formulation, the real and imaginary parts of the driving point impedance (embedding impedance) have been calculated as shown in Fig. 3*b*. The embedding impedance of the FDA has also been simulated independently using full-wave HFSS simulation. As can be seen in Fig. 3*b*, the results obtained from EOA show quite

IET Microw. Antennas Propag., 2015, Vol. 9, Iss. 11, pp. 1213–1220

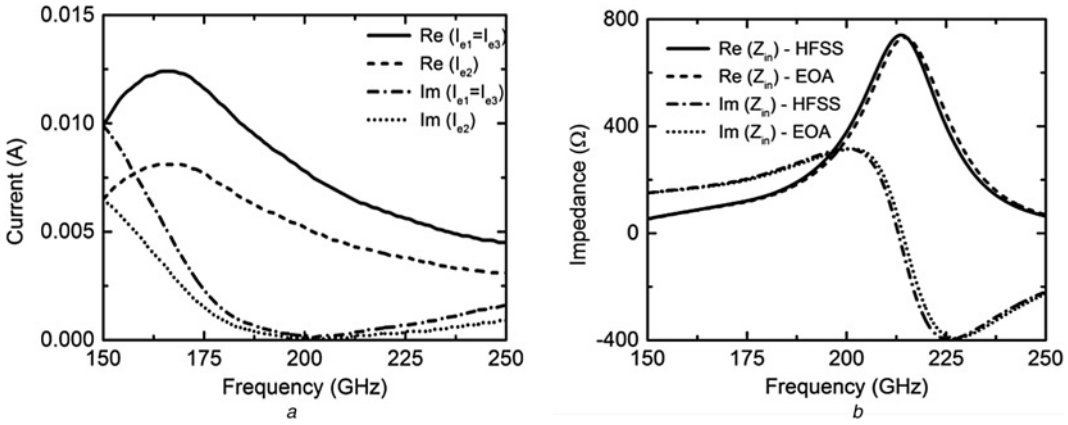

Fig. 3 *Analysis of FDAs using EOA*

a Real and imaginary parts of even-mode currents of the 200 GHz FDA for a frequency range from 150 to 250 GHz calculated using EOA
b Comparisons of simulated embedding impedance of FDA using EOA and full-wave simulations

good agreement with HFSS simulation, demonstrating the effectiveness of the proposed analysis approach.

3 LC-FDA embedding impedance

On the basis of the EOA described in Section 2, it is seen that the LC-FDA ($N = 3$) can achieve a much higher embedding impedance at its resonant frequency (i.e. 750 Ω at 215 GHz) as compared to a simple dipole antenna. According to antenna theory, the embedding impedance of a FDA is given by $Z_{in} = N^2 Z_0$, where Z_0 is the impedance of the (conventional) single dipole [26]. Owing to the above property, the proposed FDA offers additional flexibility to present a wide range of impedances by varying the antenna geometry. This provides an opportunity to conjugate match high-impedance devices, such as HBDs (e.g. typical device impedance of 124−j330 Ω [12] at 200 GHz) for maximum responsivity without additional matching networks. This approach may significantly reduce the footprint of single detectors (or imaging pixels) and enable large-scale THz FPAs.

In order to tune the embedding impedance of the FDA, the antenna geometry (i.e. N, w and g as shown in Fig. 1) needs to be adjusted. To investigate and demonstrate the tuning capacity of the antenna embedding impedance, HFSS full-wave simulations have been performed for FDAs on semi-infinite substrate with appropriate boundary conditions (since the lens dimension is much larger than that of the antenna) for a frequency range from 100 to 300 GHz, with a goal to match the HBD device impedance of ∼124−j330 Ω at 200 GHz. Fig. 4 shows the simulation results for the embedding impedance of an FDA designed with a centre frequency of ∼200 GHz by varying its number of arms, N. The antenna length was fixed at $l = 285$ µm. When N increases from 1 to 9, the real part of the impedance at resonance varies from 600 to 1800 Ω, while the maximum imaginary impedance (near resonance) ranges from 250 to 900 Ω. The effect of arm width was also investigated. Fig. 5 shows how the embedding impedance of an FDA varies with arm width w for antennas with $N = 3$ and $g = 12$ µm. As can be seen in Figs. 5*a* and *b*, as w increases from 12 to 36 µm, the real part of the antenna impedance at resonance changes from 380 to 700 Ω, while the imaginary part near resonance varies from 160 to 300 Ω. Finally, HFSS simulation results also show that the FDA impedance can be tuned by varying its arm gap from 12 to 36 µm for antennas with $N = 3$ and $w = 12$ µm. As shown in Figs. 5*c* and *d*, for g increases from 12 to 36 µm, the real part of impedance varies from 400 to 730 Ω and its imaginary part changes from 160 to 300 Ω. These results demonstrate the capability to design an FDA impedance-matched to a wide range of load impedances (e.g. ∼124−j330 Ω at 200 GHz for Sb-based HBD [12]), without the need for intervening separate matching networks. In addition, the proposed LC-FDA is also suitable for operation at higher THz frequencies. The geometry of the FDA (e.g. antenna length, arm number, arm gap and arm width) needs to be scaled and modified to achieve impedance-tuning capacity for conjugate matching with devices [15].

4 LC-FDA radiation properties

In order to achieve high directive gain and antenna efficiency, a high-resistivity (20 000 Ω·cm) silicon lens was chosen since it has

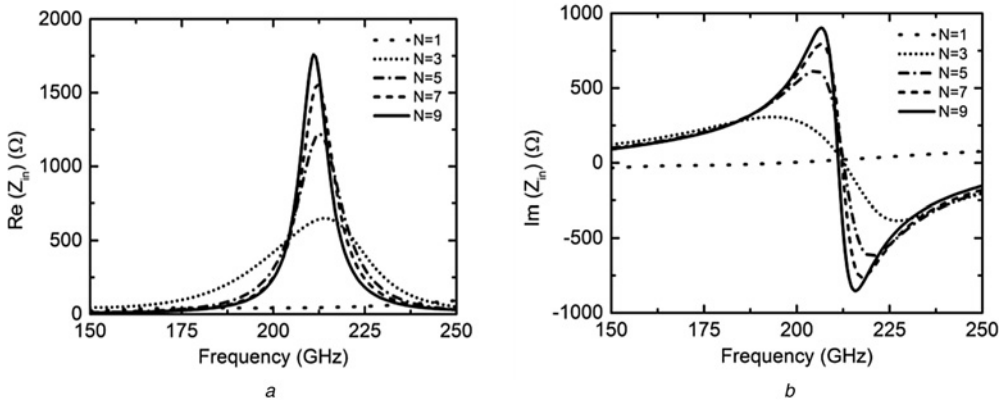

Fig. 4 *Simulation results for a FDA, showing the change in embedding impedance with antenna number of arms (N) from N = 1 to N = 9*

a Real part
b Imaginary part of antenna embedding impedance

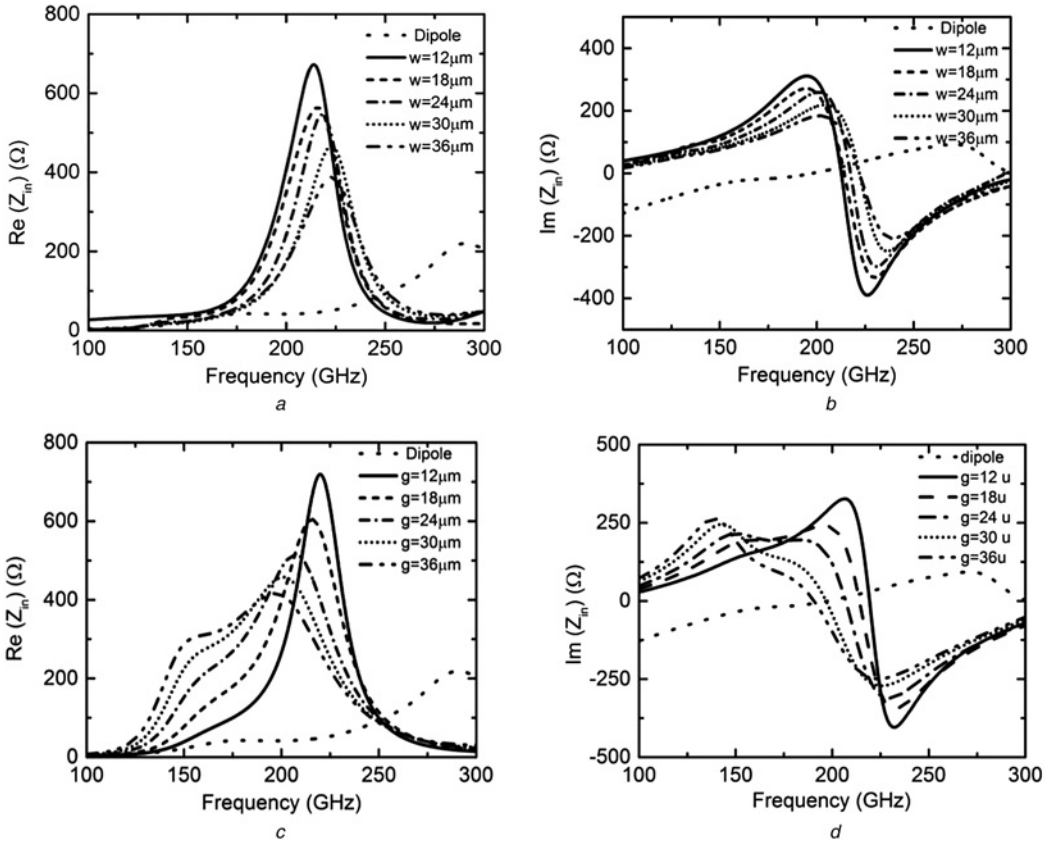

Fig. 5 *Simulation results for a FDA*

a Real part
b Imaginary part of antenna embedding impedance for FDAs ($N = 3$) with arm widths ranging from 12 to 36 μm
c Real part
d Imaginary part of antenna embedding impedance for FDAs with arm gaps ranging from 12 to 36 μm

the same dielectric constant ($\varepsilon_r = 11.7$) as the antenna substrate. If the lens and the substrate have the same dielectric constant, most of the incident rays are nearly normal to the air–dielectric interface of the curved lens surface, eliminating total internal refection and thus eliminating the associated surface waves. In addition, by utilising an extended hemispherical lens (extension length L as shown in Fig. 6), the gain and efficiency can be optimised for different applications. As noted in Section 1, the radiation properties of LC-FDAs in the THz region have not yet been fully studied and reported. For these studies, one could consider performing full-wave simulation of the complete lens-coupled antenna geometry (e.g. using HFSS), but this would require significant computer resources and long simulation times. An alternative approach is to apply the ray-tracing technique described in [10, 11]. However, application of the ray-tracing technique requires a closed-form solution for the antenna patterns without lenses. Using the EOA discussed in Section 2, an array of currents for the even (radiation) mode has already been computed; these currents are used to study the LC-FDA radiation properties using the ray-tracing technique in the following subsections.

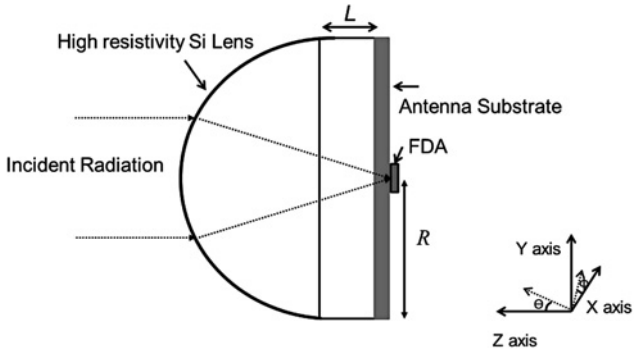

Fig. 6 *Lens-coupled FDA mounted on an extended hemispherical silicon lens of radius R and extension length L for ray-tracing analysis*

4.1 Antenna far-field radiation pattern

The far-field radiation patterns of the LC-FDA have been calculated using the ray-tracing technique [10, 11] on the basis of the EOA. If we first assume the LC-FDA is driven by a sinusoidal excitation current at the antenna feed point, then the antenna arms can be treated as an array of current sources radiating into the silicon, and the normalised element pattern inside the dielectric associated with each antenna arm is given by

$$R_n(\theta) = \frac{\sin\theta}{k_m^2 - k_e^2\cos^2\theta}\left[\cos\left(k_e l\cos\theta\right) - \cos k_m l\right] \tag{4}$$

where k_e and k_m are the propagation constants for the dielectric side and the air side, respectively, and θ is the angle with respect to the z-axis. The resultant radiation patterns of the full FDA can be calculated by including an array factor in the H-plane direction to combine the effects of each arm into the overall antenna pattern. For $N = 3$, the array factor becomes

$$A_f = I_{e2} + \left(I_{e1} + I_{e3}\right)\cos\left(k_e d\sin\theta\cos\Phi\right) \tag{5}$$

where I_{e1}, I_{e2} and I_{e3} are the radiating even-mode currents calculated using (1), d is the spacing between two adjacent arms and Φ is the

IET Microw. Antennas Propag., 2015, Vol. 9, Iss. 11, pp. 1213–1220

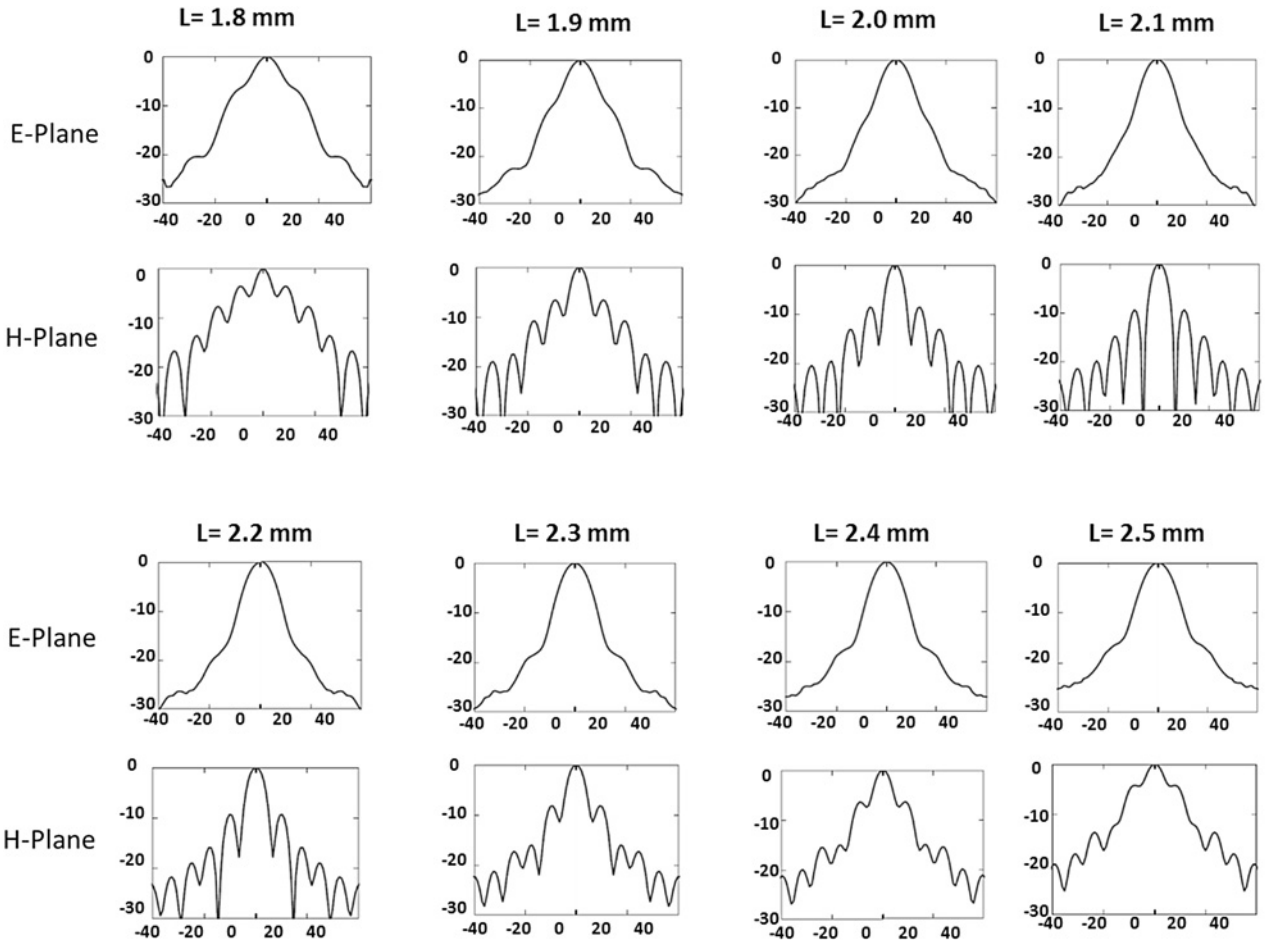

Fig. 7 *Simulated E- and H-plane radiation patterns of a 200 GHz LC-FDA with N = 3, l = 285 μm, g = 12 μm and w = 12 μm for extension lengths (L) varying from 1.8 to 2.5 mm using the ray-tracing technique*

angle from the *x*-axis in the *x*–*y* plane. Once the radiation patterns inside the dielectric medium are calculated, the far-field radiation patterns of the entire structure can be obtained from the lens surface field [10] using the ray-tracing technique. Fig. 7 shows the simulated far-field radiation patterns of the lens-coupled (R = 6 mm) FDA by varying the extension length (L) from 1.8 to 2.5 mm. It is clearly seen that the main beam of the far-field patterns in both the *E*- and *H*-planes first become narrower and then broader as the extension length is increased from 1.8 to 2.5 mm. The calculated radiation patterns in the *E*- and *H*-planes exhibit the highest directivity for a 2.2 mm extension length (or L/R ~0.37).

4.2 Antenna directivity, Gaussian coupling and radiation efficiency

The gain (or directivity) and Gaussian coupling efficiency of the lens-coupled FDA strongly depends on the lens geometry, especially the extension length (L) and radius (R) of the silicon lens. As shown in Fig. 8*a*, the directivity of the lens-coupled FDA has been calculated (on the basis of the radiation pattern calculations using the ray-tracing technique) for different lens geometries by varying both L (from 1.0 to 3.5 mm) and R (from 4 to 8 mm). For fixed lens radius, the antenna directivity initially increases and then drops as L increases. Each directivity curve (for fixed R) in Fig. 8*a* reaches a maximum approximately centred at L/R ~0.37. Similar trends have been reported in [10] for lens-coupled double-slot antennas. Although larger lens radii generally results in higher antenna directivities, Gaussian coupling efficiency (or Gaussicity, defined as the coupling efficiency of an antenna radiation pattern to the far-field pattern of an ideal Gaussian beam) must also be considered for designing an LC-FDA suitable for THz detection or imaging. As shown in Fig. 8*b*, the peak directivity increases progressively from 24 to 30 dB with an increase in lens radius from 4 to 8 mm. On the other hand, the Gaussicity of the LC-FDA decreases from 94 to 84%. For a single-pixel THz detector design using LC-FDAs, L and R should be chosen to provide the highest Gaussian coupling efficiency while still obtaining a good antenna gain (directivity). In contrast, however, higher gain/directivity (by optimising L and R) is desired in imaging FPAs to achieve high imaging resolution. In addition, HFSS simulation results have shown that the FDA on semi-infinite high-resistivity silicon substrate exhibits a radiation efficiency of 91% at 200 GHz under conjugate matching condition. The efficiency of FDA on a regular dielectric substrate with finite thickness can be improved by mounting it on an extended hemispherical lens (with same dielectric constant for reducing surface waves). The reflection loss at the air/lens (dielectric) interface can be minimised by applying a matching cap coating layer [10].

4.3 Antenna characterisation

In order to experimentally validate the antenna analysis, a 200 GHz (l = 285 μm) FDA with N = 3, arm width w = 12 μm and arm gap g = 12 μm was fabricated on a 500 μm thick high resistivity (≥20 000 Ω·cm) silicon wafer (ε_r = 11.7), using a conventional photo-lithography and Au plating process. A zero-bias Schottky diode provided by Virginia Diodes Inc. (VDI) was flip-chip mounted at the antenna feed point for use as a simple power detector (not optimised with impedance conjugate matching), as shown in Figs. 9*a* and *b*. The antenna was connected to DC output

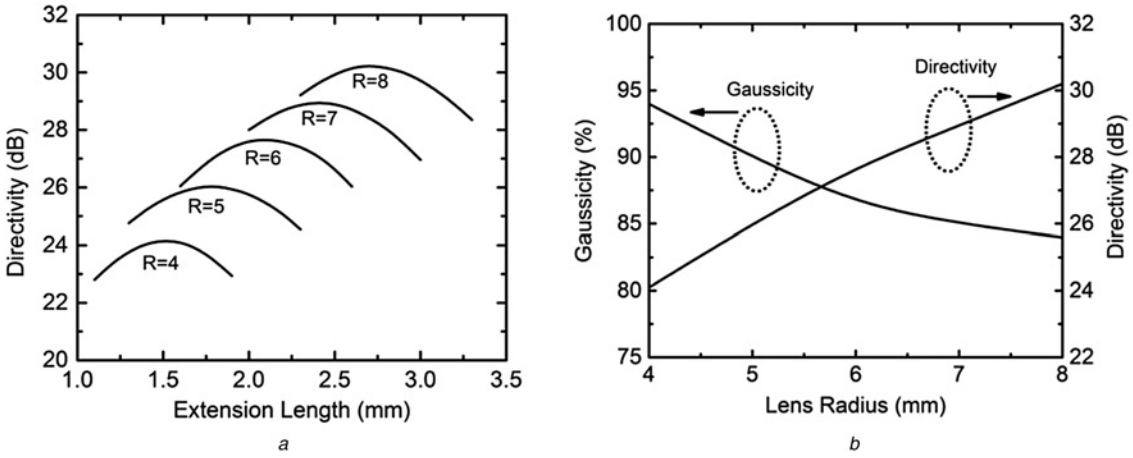

Fig. 8 *Directivity and Gaussicity calculation*

a Simulated directivity of the LC-FDA for different lens radii and extension lengths
b Simulated maximum directivity and Gaussicity for lens radii from $R = 4$ to $R = 8$ mm

pads using two meander lines. The antenna was mounted to a silicon lens with $R = 5$ mm and $L = 1.7$ mm (total extension length including the wafer thickness) for quasi-optical measurements and characterisation. The far-field radiation patterns of the LC-FDA have been measured at ~200 GHz using VDI frequency extension modules (FEMs, 190–210 GHz) for providing the THz radiation. During the measurement, the detector was mounted on a computer-controlled rotation stage. The incident RF was amplitude-modulated, and the detector output DC signal was detected and amplified using a lock-in amplifier. As shown in Figs. 9*c* and *d*, the measured radiation patterns (both the *E*- and *H*-planes) show nearly Gaussian-shaped main beams with side-lobe levels less than −14 dB. The 3-dB beam width of the folded-dipole antenna in the *H*-plane is ~10° at 200 GHz. The

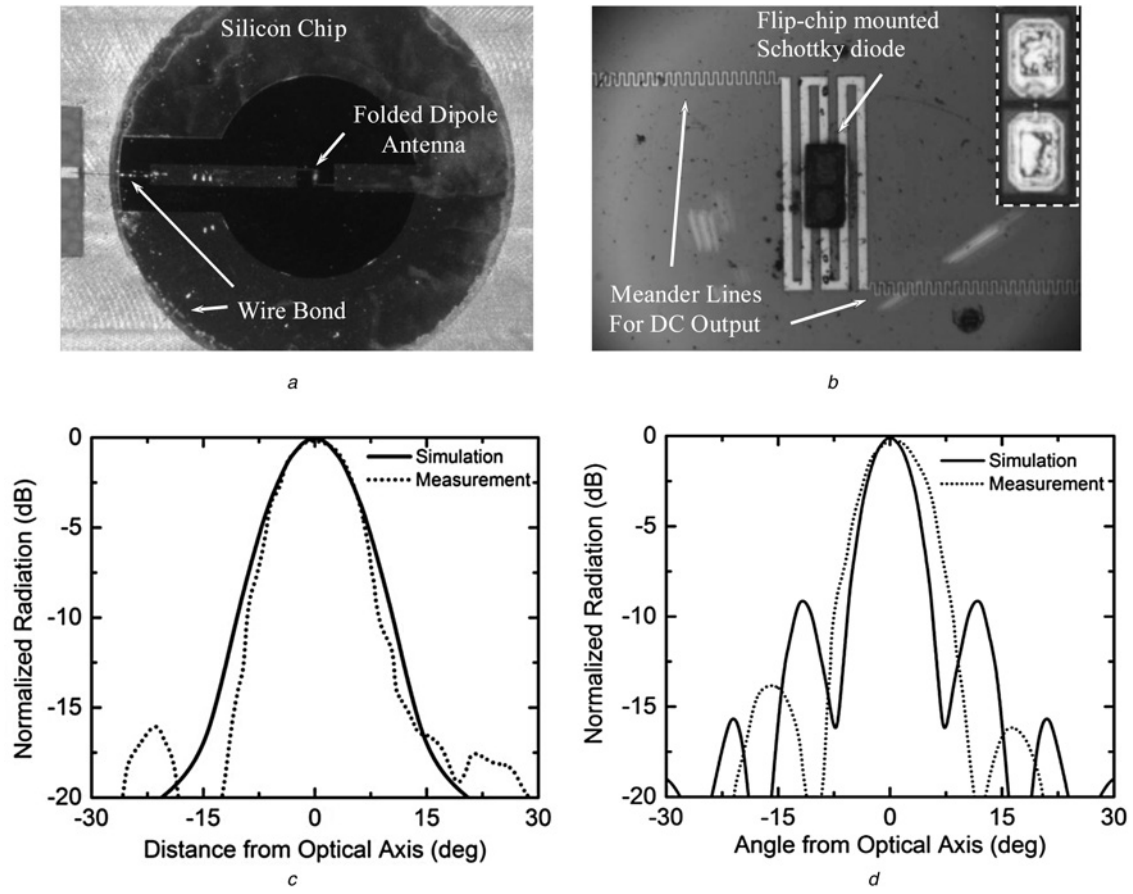

Fig. 9 *Antenna characterisation results*

a Fabricated 200 GHz FDA circuit mounted to the backside of a silicon lens for antenna characterisation
b Higher magnification view of the FDA with a flip-chip mounted zero-bias Schottky diode as a direct power detector
Inset: top view of Schottky diode
Measured and calculated radiation patterns of LC-FDA at 200 GHz
c *E*-plane
d *H*-plane

IET Microw. Antennas Propag., 2015, Vol. 9, Iss. 11, pp. 1213–1220

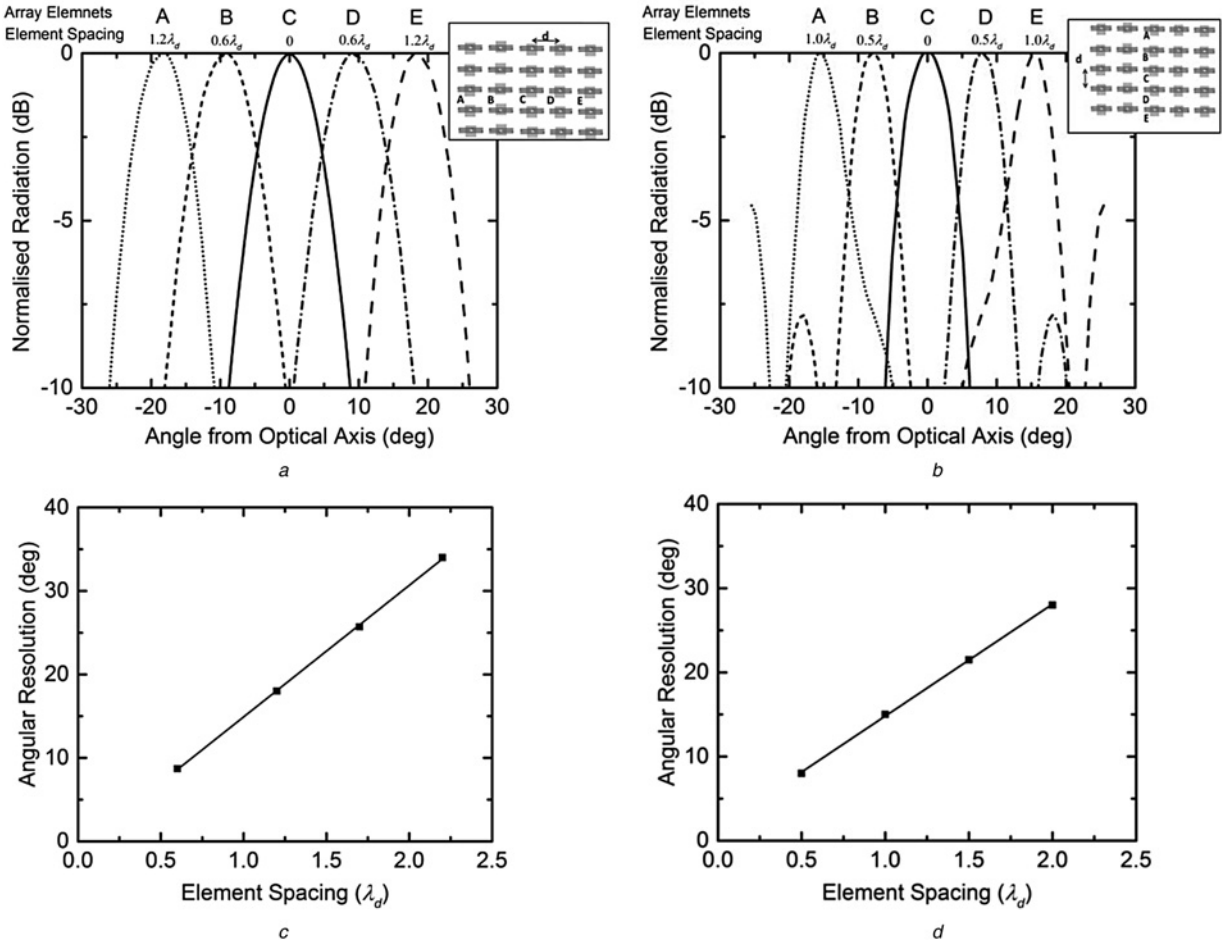

Fig. 10 *Off-axis simulation results: element radiation patterns of a LC-FDA array (5 × 5) at 200 GHz calculated using ray-tracing technique for element spacing 0.6λ_d and 0.5λ_d in the*

a E-plane
b H-plane
Angular resolution of the LC-FPA array varying with element spacing along
c E-plane
d H-plane

measured *E*-plane radiation pattern is slightly broader than the pattern in the *H*-plane, as expected [22]. Simulated results for the *E*- and *H*- plane radiation patterns are included for comparison; as can be seen, reasonably good agreement has been achieved. This indicates that the EOA approach is effective for estimating LC-FDA antenna performance. The discrepancies between the simulation and measurement results may be attributed, at least in part, to the large Schottky diode chip and the DC readout meander lines (see Fig. 9) that are present in the experimental configuration, but were not considered in the theoretical analysis. In a practical THz detector design using LC-FDAs, integrated power detection diodes (e.g. Schottky or HBD) are preferred (against the flip-chip mounting used here) and a more sophisticated DC signal output circuit [e.g. using a coplanar strip (CPS) low-pass filter structure] would be advantageous to suppress the RF currents on the DC lines [14].

5 FDA focal plane arrays for THz imaging

The design of a THz FPA using the proposed LC-FDA for imaging applications has also been evaluated. In order to evaluate the performance of the single antenna element described above in full 2-D FPAs, far-field off-axis radiation patterns [11] of the LC-FDAs have been studied for a 5 × 5 array. Figs. 10*a* and *b* show the off-axis radiation patterns along the *E*- and *H*-planes. The array element pattern in the *E*-plane has a 3-dB beam width of $\theta_{3\text{-dB}}$ ~8.2° with side-lobe levels less than −15 dB. The main beam spacing between adjacent antennas is $\Delta\theta$ ~8.7° with a crossover power level of −3 dB for an antenna distance $d = 0.6\lambda_d$, where λ_d is the guided wavelength, as shown in Fig. 10*a*. In the *H*-plane patterns shown in Fig. 10*b*, the element pattern has $\theta_{3\text{-dB}}$ ~6°, $\Delta\theta$ ~8° and a crossover power level of −4 dB for $d = 0.5\lambda_d$. The angular resolution, which is limited by a single pixel (FDA) size and determined by beam spacing, has been calculated for element spacing varying from 0.6λ_d to 2.2λ_d and 0.5λ_d to 2.0λ_d in the *E*-and *H*-planes, respectively. Figs. 10*c* and *d* show that the angular resolution increases linearly with decreasing element spacing in both the *E*- and *H*-planes. The calculated highest angular imaging resolution in the *E*-and *H*-planes are 8.7° and 6.8° for element spacing 0.6λ_d to 0.4λ_d (limited by the FDA dimensions), respectively. However, the imaging contrast may become worse with increased angular resolution, especially when crossover power level becomes less than 3 dB (see Figs. 10*c* and *d*). Thus, a trade-off between imaging resolution and contrast must be made by selecting the appropriate element spacing in the 2D THz FPA.

6 Conclusions

LC-FDAs have been evaluated for THz detection and imaging applications. EOA was performed to analyse the antennas and extract the mode currents for determining the embedding

impedance and facilitating radiation property calculations. The antenna embedding impedance was studied for different antenna geometries; the results show that a wide range of impedance values (both real and imaginary parts) can be achieved. This unique property makes LC-FDAs especially attractive for high-performance THz detectors in which impedance matching between antennas and small-area detectors is required. On the basis of the currents calculated using EOA, the LC-FDA far-field radiation patterns, antenna directivity and Gaussian coupling efficiency for different lens structures have been studied using the ray-tracing technique. Good agreement between calculation results and experimental measurements has been obtained, demonstrating the effectiveness of the above analysis. In order to evaluate the FDAs for 2D THz FPAs with high imaging resolution, the lens structure has been optimised and the off-axis radiation patterns of the FPAs are evaluated. The results suggest that LC-FDAs are promising for realising high-performance THz detectors and FPAs.

7 Acknowledgments

This work was supported by the National Science Foundation (NSF) under grants ECCS-1002088 and ECCS-1102214. The authors thank the staff of the Notre Dame Nanofabrication (NDNF) facility for discussions and assistance. The authors also acknowledge the support of the Advanced Diagnostics and Therapeutics Initiative (AD&T) and Notre Dame's Center for Nano Science and Technology (NDnano) at the University of Notre Dame.

8 References

1 Siegel, P.H.: 'THz technology in biology and medicine', *IEEE Trans. Microw. Theory Tech.*, 2004, **52**, (10), pp. 2438–2448
2 Rutledge, D.B., Muha, M.S.: 'Imaging antenna arrays', *IEEE Trans. Antennas Propag.*, 1982, **30**, (2), pp. 535–540
3 Mittleman, D., Gupta, M., Neelamani, R., Baraniuk, R., Rudd, J., Koch, M.: 'Recent advances in terahertz imaging', *Appl. Phys. B, Lasers Opt.*, 1999, **68**, pp. 1085–1094
4 Cooper, K.B., Dengler, R.J., Llombart, N., Thomas, B., Chattopadhyay, G., Siegel, P.H.: 'THz imaging radar for standoff personnel screening', *IEEE Trans. THz Sci. Tech.*, 2011, **1**, (1), pp. 169–182
5 Sobis, P.J., Emrich, A., Stake, J.: 'A low VSWR 2SB Schottky receiver', *IEEE Trans. THz Sci. Tech.*, 2011, **1**, (2), pp. 403–411
6 Burdette, D.J., Alverbro, J., Zhang, Z., *et al.*: 'Development of an 80 × 60 pixel, broadband, real-time THz imager'. SPIE Proc., 2011, vol. 8023
7 Kannegulla, A., Jiang, Z., Rahman, S., *et al.*: 'Coded-aperture imaging using photo-induced reconfigurable aperture arrays for mapping terahertz beams', *IEEE Trans. THz Sci. Tech.*, 2014, **4**, (3), pp. 321–327
8 Shams, M.I.B., Jiang, Z., Rahman, S., *et al.*: 'Approaching real-time THz imaging using photo-induced coded apertures and compressed sensing', *Electron. Lett.*, 2014, **50**, (11), pp. 801–803
9 Sensale-Rodriguez, B., Rafique, S., Yan, R., *et al.*: 'Terahertz imaging employing graphene modulator array', *Opt. Express*, 2013, **21**, (2), pp. 2324–2330
10 Filipovic, D.F., Gearhart, S.S., Rebeiz, G.M.: 'Double-slot antennas on extended hemispherical and elliptical silicon dielectric lenses', *IEEE Trans Microw. Theory Tech.*, 1993, **41**, (10), pp. 1738–1749
11 Filipovic, D.F., Gearhart, S.S., Rebeiz, G.M.: 'Off-axis properties of silicon and quartz dielectric lens antennas', *IEEE Trans. Antennas Propaga.*, 1997, **45**, (5), pp. 760–766
12 Liu, L., Xu, H., Lichtenberger, A.W., Weikle II, R.M.: 'Integrated 585 GHz hot-electron mixers and focal-plane arrays based on annular slot antennas', *IEEE Trans. Microw. Theory Tech.*, 2010, **58**, (7), pp. 1943–1951
13 Rahman, S.M., Jiang, Z., Xie, Y., Xing, H.G., Fay, P., Liu, L.: 'Terahertz focal-plane arrays employing heterostructure backward diodes integrated with folded dipole antennas'. IEEE Int. Microwave Symp., USA, Seattle, June 2013
14 Rahman, S.M., Xie, Y., Jiang, Z., Xing, H.G., Fay, P., Liu, L.: 'Development of terahertz focal plane array elements using Sb-based heterostructure backward diodes'. 23rd Int. Symp. Space Terahertz Tech., Japan, Tokyo, April 2012
15 Rahman, S.M., Jiang, Z., Xing, H.G., Fay, P., Liu, L.: 'Design, fabrication and characterization of 585 GHz integrated focal-plane arrays based on heterostructure backward diodes'. 39th Int. Conf. on Infrared, Millimeter, and Terahertz Waves, USA, Arizona, September 2014
16 Liu, L., Hesler, J.L., Xu, H., Lichtenberger, A.W., Weikle, R.M.: 'A broadband quasi-optical terahertz detector utilizing a zero bias Schottky diode', *IEEE Microw. Wirel. Compon. Lett.*, 2010, **20**, (9), pp. 504–506
17 Hsu, P.L., Deng, B.H., Wang, J., Domier, C.W., Luhmann, N.C.Jr.: 'Millimeter-wave imaging array development for microwave reflectometry and ECE imaging', *Rev. Sci. Instrum.*, 2001, **72**, (1), pp. 364–367
18 Ganzevles, W.F.M., Swart, L.R., Gao, J.R., de Korte, P.A.J., Klapwijk, T.M.: 'Direct response of twin-slot antenna-coupled hotelectron bolometer mixers designed for 2.5 THz radiation detection', *Appl. Phys. Lett.*, 2000, **76**, (22), pp. 3304–3306
19 Jiang, Z., Rahman, S., Hesler, J.L., Fay, P., Liu, L.: 'Design and characterization of tunable lens-coupled annular-slot antennas for all-electronic reconfigurable THz detectors and focal-plane arrays', *IET Microw. Antennas Propag.*, 2014, **8**, (11), pp. 842–848
20 Jiang, Z., Rahman, S.M., Fay, P., Hesler, J.L., Liu, L.: 'Tunable 200 GHz lens-coupled annular-slot antennas using Schottky varactor diodes for all-electronic reconfigurable terahertz circuits', *Electron. Lett.*, 2013, **49**, (23), pp. 1428–1430
21 Semenov, A.D., Richter, H., Hubers, H.-W., *et al.*: 'Terahertz performance of integrated lens antennas with a hot-electron bolometer', *IEEE Trans. Microw. Theory Tech.*, 2007, **55**, (2), pp. 239–247
22 Rebeiz, G.M.: 'Millimeter-wave and terahertz integrated circuit antennas', *Proc. IEEE*, 1992, **80**, pp. 1748–1779
23 Fay, P.: 'High performance heterostructure backward diode detectors'. SPIE Defense and Security Conf., USA, Orlando, April 2011
24 Zhang, Z., Rajavel, R., Deelman, P., Fay, P.: 'Sub-micron area heterojunction backward diode millimeter-wave detectors with 0.18 pW/Hz$^{1/2}$ noise equivalent power', *IEEE Microw. Wirel. Compon. Lett.*, 2011, **21**, (5), pp. 267–269
25 Liu, L., Xu, H., Duan, Y., Lichtenberger, A.W., Hesler, J.L., Weikle II, R.M.: 'A 200 GHz Schottky diode quasi-optical detector based on folded dipole antenna'. 20th Int. Symp. on Space Terahertz Tech., USA, Charlottesville, April 2009
26 Balanis, C.A.: 'Antenna theory: analysis and design' (John Wiley & Sons, Inc., Hoboken, NJ, 2005, 3rd edn.), pp. 515–521
27 Moon, K., Han, H., Park, I.: 'Terahertz folded half-wavelength dipole antenna for high output power'. Topical Meeting Microwave Photonics, Korea, Seoul, 2005, pp. 301–304
28 Endo, T., Sunahara, Y., Satoh, S., Katagi, T.: 'Resonant frequency and radiation efficiency of meander line antennas', *Electron. Commun. Jpn II. Electron.*, 2000, **83**, (1), pp. 52–58
29 Montero-de-Paz, J., Ugarte-Munoz, E., Garcia-Munoz, L.E., Camara Mayorga, I., Segovia-Vargas, D.: 'Meander dipole antenna to increase CW THz photomixing emitted power', *IEEE Trans. Antennas Propaga.*, 2014, **62**, (9), pp. 4868–4872
30 Montero-de-Paz, J., Ugarte-Muñoz, E., Garcia-Muñoz, L.E., *et al.*: 'Millimeter-wave receiver based on a folded dipole antenna and Schottky diode for maximum power transfer'. EuCAP, Czech Republic, Prague, March 2012, pp. 1259–1262
31 Lampe, R.W.: 'Design formulas for an asymmetric coplanar strip folded dipole', *IEEE Trans. Ant. Propag.*, 1985, **33**, (9), pp. 1028–1031